Cell Reports
Physical Science

Article

Scalable flame spray-derived bismuth catalysts enable efficient CO_2 electrolysis revealed by FIB-SEM nano-tomography and ICP-MS EDX profiling

Graphical abstract

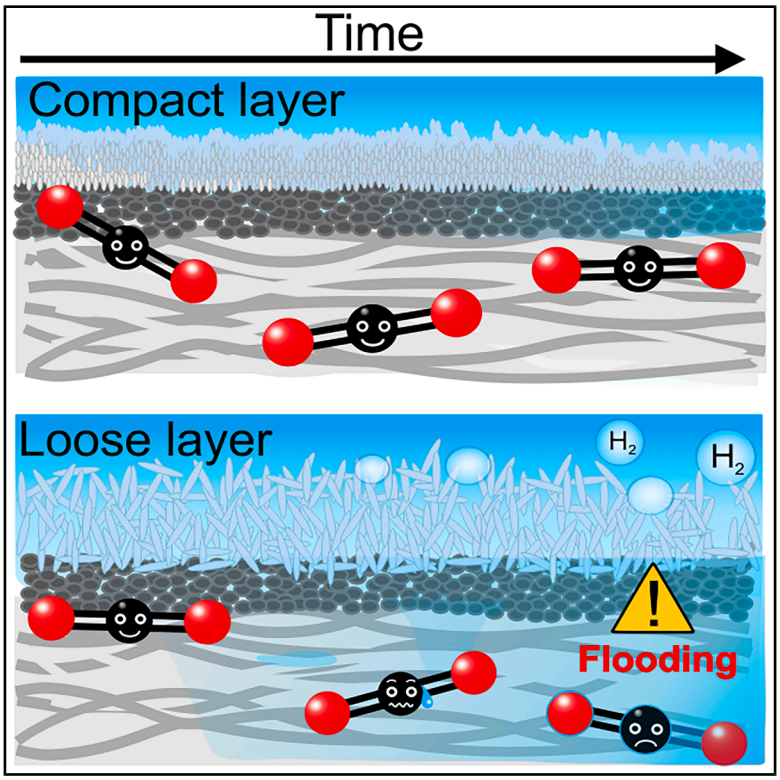

Authors

Alain Rieder, Hesamoddin Rabiee, Francesca Lorenzutti, ..., Wendelin Stark, Sophia Haussener, Peter Broekmann

Correspondence

hesamoddin.rabiee@unibe.ch

In brief

Rieder et al. explore how flame spray pyrolysis-derived bismuth oxide catalysts outperform electrodeposited dendritic analogs for carbon dioxide electrolysis to formate. Combined nano-tomography and elemental profiling reveal how compact catalyst layers delay gas diffusion electrode flooding, suppress catalyst degradation, and improve durability at industrially relevant current densities.

Highlights

- Nano-tomography profiling was used to study electrode degradation in CO_2 electrolysis
- Electrode flooding is temporally linked with H_2 evolution and catalyst dissolution
- Flame spray bismuth oxide reaches >90% formate selectivity from CO_2 electrolysis
- The origin of bismuth oxide determines the electrolysis performance and stability

Rieder et al., 2026, Cell Reports Physical Science 7, 103500
September 16, 2026
https://doi.org/10.1016/j.xcrp.2026.103500

CellPress

Cell Reports
Physical Science

CellPress
OPEN ACCESS

Article

Scalable flame spray-derived bismuth catalysts enable efficient CO_2 electrolysis revealed by FIB-SEM nano-tomography and ICP-MS EDX profiling

Alain Rieder,[1,2] Hesamoddin Rabiee,[1,2,7,*] Francesca Lorenzutti,[2,3] Patrik Willi,[2,4] Lucas Warmuth,[5] Soma Vesztergom,[6] Robert Grass,[2,4] Wendelin Stark,[2,4] Sophia Haussener,[2,3] and Peter Broekmann[1,2]

[1]Department of Chemistry, Biochemistry and Pharmaceutical Sciences, University of Bern, Freiestrasse 3, 3012 Bern, Switzerland
[2]NCCR Catalysis, Switzerland
[3]Laboratory of Renewable Energy Science and Engineering, Swiss Federal Institute of Technology in Lausanne (EPFL), 1015 Lausanne, Switzerland
[4]Functional Materials Laboratory, Institute of Chemical and Bioengineering, Department of Chemistry and Applied Biosciences, ETH Zurich, Vladimir-Prelog-Weg 1, 8093 Zurich, Switzerland
[5]Institute of Catalysis Research and Technology (IKFT), Karlsruhe Institute of Technology (KIT), Hermann-von-Helmholtz-Platz 1, 76344 Eggenstein-Leopoldshafen, Germany
[6]MTA-ELTE Momentum Interfacial Electrochemistry Research Group, Eötvös Loránd University, Pázmány Péter Sétány 1/A, 1117 Budapest, Hungary
[7]Lead contact
*Correspondence: hesamoddin.rabiee@unibe.ch
https://doi.org/10.1016/j.xcrp.2026.103500

SUMMARY

CO_2 electrolysis is a promising route to convert CO_2 into value-added chemicals. Here, we use flame spray pyrolysis (FSP) as a rapid and scalable method to synthesize Bi_2O_3 nanospheres and evaluate their formate production in a gas diffusion electrode flow electrolyzer. Under reaction conditions, Bi_2O_3 converts *in situ* into bismuth subcarbonate, delivering >90% formate Faradaic efficiency across −0.6 to −1.6 V vs. reversible hydrogen electrode (RHE), reaching a formate partial current density of −700 mA.cm^{-2} at −1.8 V. This performance is nearly twice that of electrochemically deposited dendritic Bi_2O_3. To elucidate the origin of this high performance, a combined tomography approach based on focused ion beam-scanning electron microscopy (FIB-SEM) nano-tomography and inductively coupled plasma-mass spectrometry (ICP-MS) EDX cross-sectional profiling was introduced to track catalyst layer morphology and electrolyte-induced flooding. The FSP-derived catalyst forms a compact layer near the microporous layer, confining flooding to the catalyst microporous interface and improving operational stability. This work provides mechanistic insight and characterization guidelines for designing durable, high-performance electrodes for CO_2 electrolysis.

INTRODUCTION

The continuous rise in anthropogenic CO_2 emissions and global temperatures intensifies the need for mitigation strategies that lower industrial carbon footprints and enable renewable energy storage.[1] Among the proposed approaches, carbon capture combined with the electrochemical (EC) CO_2 reduction reaction (ECO_2RR), powered by renewable energy sources, offers a promising and potentially scalable route to mitigate CO_2 emissions while producing value-added chemicals.[2–4] Over recent decades, the ECO_2RR has progressed from fundamental studies toward industrial relevance.[5–9] Extensive efforts have focused on developing active and selective catalyst materials: Au and Ag show high efficiencies for CO production,[10,11] whereas Cu favors C_{2+} products,[7,12] while Bi and Sn exhibit higher selectivity toward formate.[13] Bismuth, in particular, has attracted considerable interest because it is non-toxic, inexpensive, and Earth abundant. Its low affinity for adsorbed hydrogen (H*) suppresses the competing HER, thereby enhancing its suitability for the ECO_2RR.[14–16] Importantly, Bi uniquely incorporates CO_2 into its oxide lattice to form bismuth subcarbonate ($(BiO)_2CO_3$), a highly active catalyst for formate production,[17–19] and our previous study provided direct evidence for this transition via *operando* Raman spectroscopy.[18]

H-type cell experiments have been crucial for advancing the fundamental understanding of the ECO_2RR and enabling the discovery of new catalysts. However, they face inherent limitations: in particular, the low solubility of CO_2 in aqueous electrolytes restricts the achievable current density to a mass-transport limit that is typically two orders of magnitude below the industrially relevant range (> −0.5 to −1 A cm^{-2}).[20,21] To increase operational current density, flow-cell electrolyzers equipped with gas

diffusion electrodes (GDEs) have emerged as a promising strategy, as they improve delivery of CO_2 to the catalyst surface.[22,23] GDEs typically comprise three layers: (1) a conductive carbon fiber layer (CFL) that provides mechanical stability and electrical conductivity; (2) a hydrophobic microporous layer (MPL), often enriched with polytetrafluoroethylene (PTFE), together with the CFL forming the gas diffusion layer (GDL) or substrate; and (3) a catalyst layer interfaced with the MPL, where CO_2 reduction occurs.[24,25]

Although flow cells enable operation at industrially relevant current densities, they introduce new challenges, particularly for GDE stability.[26,27] Therefore, electrode durability remains a critical bottleneck for economically viable ECO_2RRs. One of the key degradation mechanisms is electrolyte flooding of the GDE, which limits CO_2 access to the catalyst.[27] Bismuth-based catalysts are especially sensitive to CO_2 depletion; under such conditions, the active bismuth subcarbonate phase is reduced to metallic bismuth, leading to a pronounced loss in formate selectivity.[28,29] The accumulated catholyte inside the GDE can penetrate the CO_2 flow field and leave the cell as droplets. This "electrolyte perspiration" through the GDE into the gas compartment regulates flooding and can delay complete catalytic failure.[30,31] Efficient electrolyte management therefore requires careful GDE design. One strategy is to employ non-conductive, hydrophobic substrates such as PTFE or poly(vinylidene fluoride) (PVDF) as GDLs, which are resistant to electrowetting.[32–34] Another approach is increasing the hydrophobicity of the catalyst layer by tuning the ionomer or adding hydrophobic nanoparticles (e.g., PTFE).[35–38] In recent years, several methods have been developed to observe and quantify flooding in GDEs under ECO_2RR conditions. Synchrotron-based *operando* techniques, although requiring specialized cell designs, provide detailed insight into GDE wetting behavior,[39,40] while perspiration analysis offers a complementary route to monitor and quantify electrolyte transport and retention.[25,41,42]

The reproducible and rapid synthesis of catalyst materials with well-defined composition and morphology is essential for implementing the ECO_2RR at an industrially relevant scale.[43] Different synthesis routes generate distinct particle sizes and morphologies, which strongly influence EC performance. Conventional lab-scale nanoparticle syntheses are typically constrained by low production rates. Dynamic hydrogen bubble template (DHBT) electrodeposition is widely used to produce high-surface-area foams of fine particles, but despite being well established and reproducible, it is generally limited to deposition rates of $\sim$10 μg min^{-1} (per 1 A m^{-2}).[44] In contrast, flame spray pyrolysis (FSP) enables highly efficient nanoparticle production at rates exceeding 10 g min^{-1},[45,46] offering a realistic pathway toward mass fabrication of GDEs for the ECO_2RR.[47] To date, a systematic understanding of how the structural characteristics of DHBT- and FSP-derived GDEs influence their catalytic evolution and susceptibility to flooding remains lacking, and a direct comparative analysis has not yet been reported. This gap complements the broader body of research, which has primarily focused on the optimization of active catalyst materials.

In this work, Bi_2O_3 particles with distinct sizes and morphologies are synthesized by FSP (FSP Bi_2O_3) and DHBT EC deposition (EC Bi_2O_3). The small, spherical FSP Bi_2O_3 particles exhibit markedly enhanced ECO_2RR performance compared to the larger, dendritic EC Bi_2O_3 structures, achieving formate selectivities above 90% over a broad potential window of −0.6 to −1.6 V vs. reversible hydrogen electrode (RHE), vs. −0.6 to −1.2 V vs. RHE for EC Bi_2O_3. FSP Bi_2O_3 also shows superior activity, reaching formate partial current densities (PCDs) exceeding −700 mA cm^{-2}, compared to −396 mA cm^{-2} for EC Bi_2O_3. Performance losses at current densities above −500 mA cm^{-2} are investigated using focused ion beam-scanning electron microscopy (FIB-SEM) nano-tomography in combination with previously established inductively coupled plasma-mass spectrometry (ICP-MS) EDX (energy-dispersive X-ray) cross-sectional profiling, enabling detailed analysis of catalyst degradation and substrate flooding. The FSP Bi_2O_3 GDEs form a compact catalyst layer from the smaller FSP-derived particles, which mitigate flooding over an extended potential window and operating time, thereby maintaining superior electrocatalytic performance compared to EC Bi_2O_3.

RESULTS AND DISCUSSION

Catalyst and GDE preparation and characterization

The two synthesis methods, FSP and EC, were employed to obtain distinct Bi_2O_3 catalyst precursors (schematic illustrations in Figures 1A and 1B). In FSP, a suitable bismuth precursor was dissolved in an organic solvent and sprayed into a reactor, where combustion of the microdroplets in an oxygen atmosphere produced aggregates of spherical primary particles (FSP Bi_2O_3), which were collected on a glass fiber filter at the top of the reactor.[48] Dendritic Bi_2O_3 was synthesized via DHBT (EC Bi_2O_3) at a high current density (−3 A cm^{-2}), leading to simultaneous hydrogen evolution and Bi foam formation (Figure S1),[35] followed by mechanical removal by sonication and subsequent oxidation in a furnace to yield bismuth oxide (Bi_2O_3). The average particle deposition rate for EC deposition was gravimetrically determined to be 420 mg h^{-1}, more than an order of magnitude lower than that of the FSP process (10–20 g h^{-1}). Brunauer–Emmett–Teller (BET) N_2 adsorption revealed that FSP Bi_2O_3 has a $\sim$2.5-fold higher specific surface area than EC Bi_2O_3 (9.3 vs. 3.7 m^2 g^{-1}; isotherms in Figure S2). High-resolution TEM (HRTEM) images of both materials showed lattice spacings of $\sim$0.314 nm corresponding to the [210] plane of Bi_2O_3 (Figures 1C and 1D).

GDEs were fabricated by airbrushing the catalyst ink (details in the supplemental information) onto Freudenberg H23C8 GDLs (SEM in Figure S3). Dynamic light scattering (DLS) of the freshly prepared inks showed particle size distributions of 360–586 nm for EC Bi_2O_3 and 160–330 nm for FSP Bi_2O_3 (Figure 2A). The larger apparent size of FSP Bi_2O_3 compared to HRTEM results arises from particle agglomeration, which was observed at the GDE edges by SEM (Figures S4A and S4B). While the spherical FSP Bi_2O_3 particles can penetrate and embed within the small pores of the MPL, the larger dendritic EC Bi_2O_3 structures predominantly interact with the MPL surface (Figure S4C). Surface imaging of the GDEs revealed a homogeneous yellow catalyst layer without visible cracks down to the MPL interface (Figures 2B, 2C, and S5A; SEM in Figures 2D, 2E, and S6), as observed in our previous works.[28,29] Small deposits of catalyst

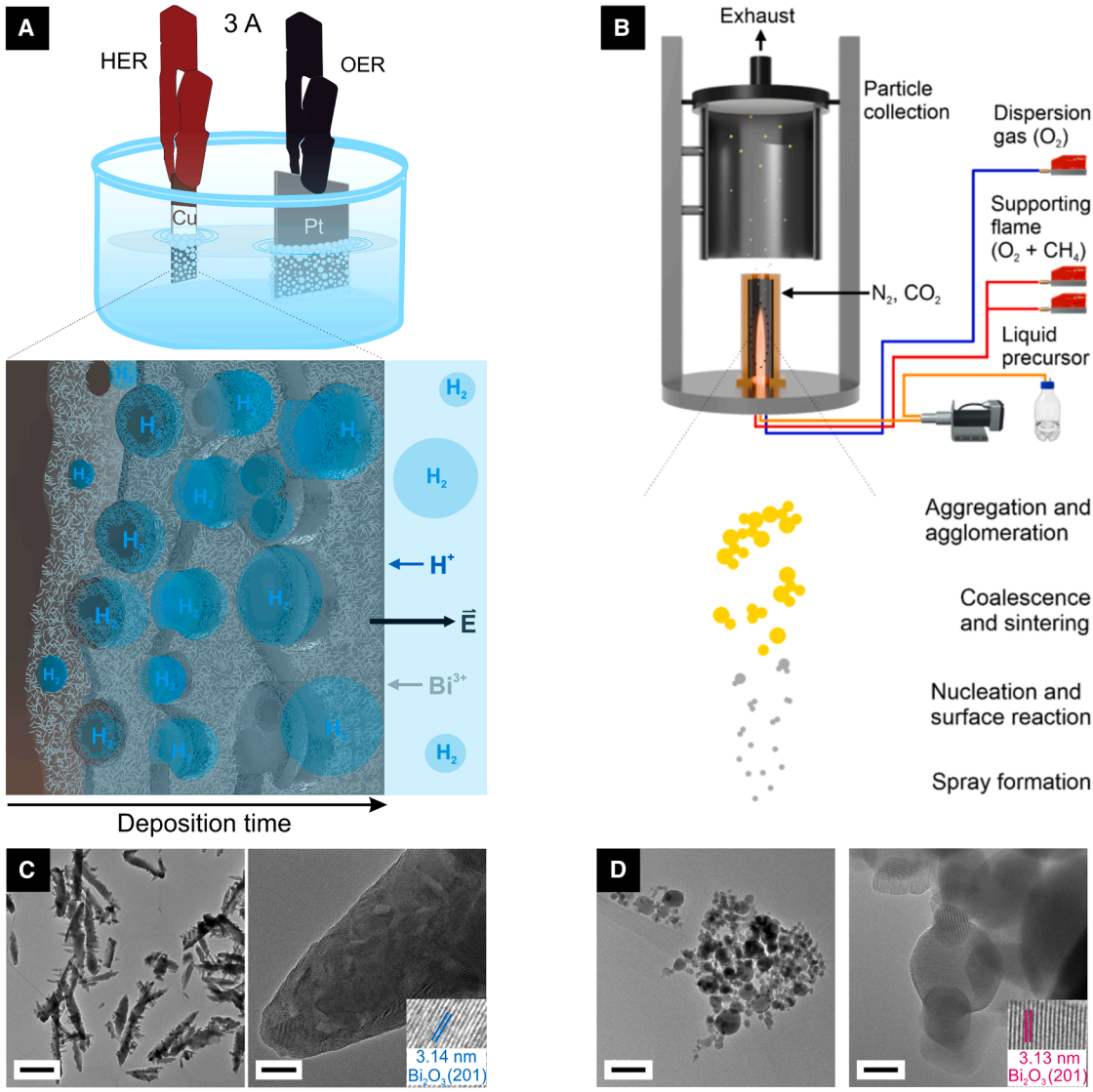

Figure 1. Schematic illustration of the experimental setup and catalyst precursor preparation

(A) DHBT electrodeposition: magnified regions show foam formation at different deposition times, with H_2 bubbles guiding metal deposition.

(B) FSP: the liquid precursor feed is dispersed at a nozzle by controlled O_2 flow, and the resulting spray is ignited by a premixed supporting flame.

(C) HRTEM image and lattice spacing of the EC-derived dendritic Bi_2O_3 (scale bar in TEM images: 750 nm [left] and 15 nm [right]).

(D) HRTEM image and lattice spacing of the FSP-derived spherical Bi_2O_3 particles (scale bar in TEM images: 100 nm [left] and 15 nm [right]).

material were detected at the back-side edges of the GDE and transported through a narrow gap between the GDE and the filter holder (Figures S5B–S5D). The gravimetrically determined average mass loading of the fresh GDEs was 1.1 ± 0.05 mg cm^{-2}. Cross-sectional SEM-EDX images (Figures 2F–2I) and optical micrographs (Figure S7) showed a compact catalyst layer on top of the MPL, with average thicknesses of ~6.06 μm for EC Bi_2O_3 and ~3.41 μm for FSP Bi_2O_3. X-ray diffraction (XRD) diffractograms of the films exhibited identical 2θ values corresponding to β-Bi_2O_3 (JPCDS file no. 41-1449), with the most intense reflection at 27.38° assigned to the [210] lattice plane (Figure 2J), consistent with previous reports.[18,29] The Rietveld refinement indicates that both materials are fully oxidized, with less than 1% metallic Bi present. Raman spectroscopy (Figure 2K) confirmed the presence of bismuth oxide via the characteristic Bi_2O_3 band at 313 cm^{-1}. A small shoulder at 162 cm^{-1} was assigned to bismuth subcarbonate ($(BiO)_2CO_3$), formed by the reaction of Bi_2O_3 with atmospheric CO_2. ICP-MS impurity screening of both samples revealed negligible traces of Cu, Fe, Ni, Sn, and Pb.

The hydrophobicity of the catalyst layer is a key parameter for electrolyte management and flooding mitigation in GDEs.[35,49–51] Contact angle (CA) measurements of the as-prepared coatings showed superhydrophobic behavior for both samples, with

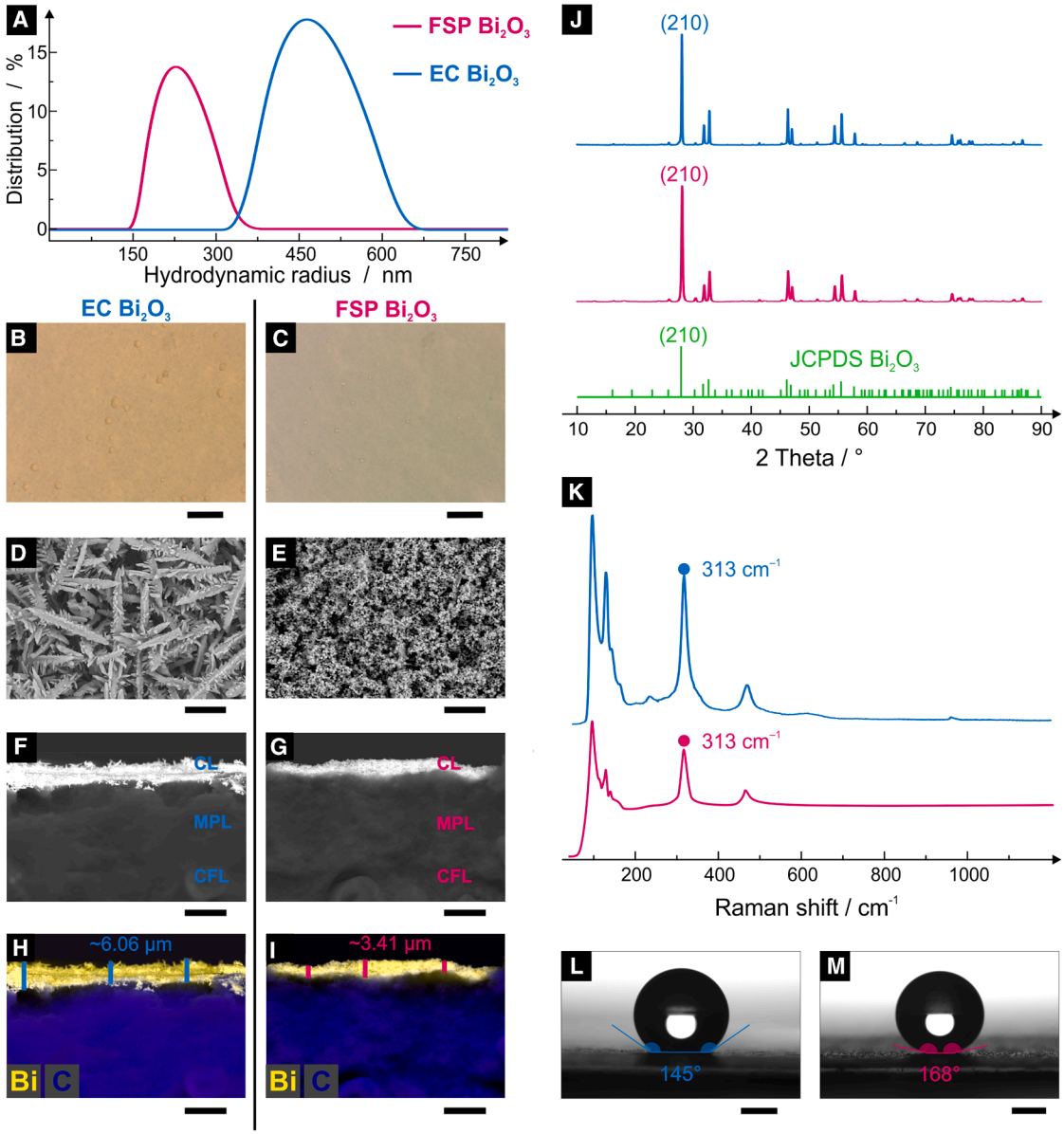

Figure 2. Physical and chemical characterization of as-prepared EC Bi_2O_3 and FSP Bi_2O_3 GDEs

Physical and chemical characterization of as-prepared EC Bi_2O_3 (blue) and FSP Bi_2O_3 (pink) GDEs.
(A) Nanoparticle size distributions of the catalyst inks from DLS.
(B and C) 3D microscope images of the catalyst layers.
(D and E) Surface SEM images of the catalyst morphologies.
(F–I) Cross-sectional SEM-EDX analysis of the catalyst and microporous layers.
(J and K) XRD patterns with Bi_2O_3 reference and Raman spectra of the catalyst films.
(L and M) Contact angle measurements of the films prepared with Nafion as binder.
Scale bars: 300 μm for (B) and (C), 1 μm for (D) and (E), 10 μm for (F)–(I), and 1 mm for (L) and (M).

CAs of 145° for EC Bi_2O_3 and 168° for FSP Bi_2O_3 (Figures 2L and 2M). As both catalyst layers consist of the same material and were prepared using identical procedures, the difference in CA is most likely attributed to variations in particle size and the resulting surface roughness.[52] To probe the role of the ionomer, sessile-drop measurements were performed on catalyst films without Nafion. In the absence of Nafion, the EC Bi_2O_3 GDE exhibited a significantly lower CA than the FSP Bi_2O_3 GDE (85° vs. 143°; Figure S8), indicating higher wettability. The negligible dependence of FSP Bi_2O_3 GDE hydrophobicity on Nafion content suggests that its wetting behavior is dominated by particle size and morphology rather than binder composition.

The freshly prepared GDEs were then mounted into the flow electrolyzer (Figure S9) for EC testing. To assess CO_2

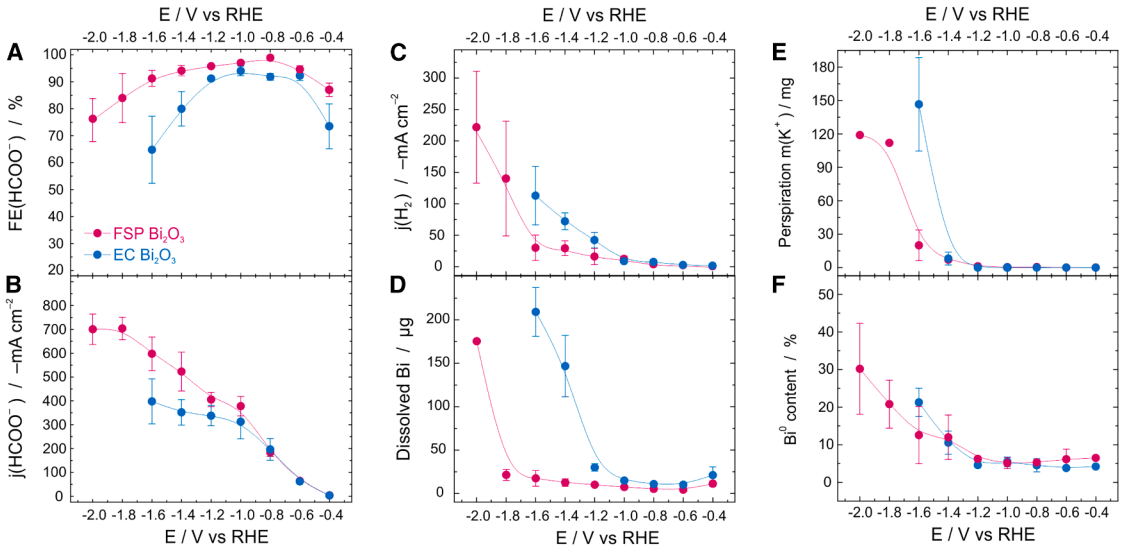

Figure 3. Potential-dependent ECO_2RR performance and characterization of EC Bi_2O_3 and FSP Bi_2O_3 catalysts

(A and B) Faradaic efficiencies and partial current densities of formate. Data are represented as mean ± SEM (n = 3).

(C) Partial current densities of H_2 for both catalysts. Data are represented as mean ± SEM (n = 3).

(D and E) ICP-MS quantification of K^+ in the perspired electrolyte collected in the trap and Bi^{3+} dissolved in the catholyte. Data are represented as mean ± SEM (n = 3).

(F) Metallic Bi content determined by XRD as a function of applied potential. Data are represented as mean ± SEM (n = 3).

permeability, Ar was introduced into the catholyte chamber at 25 mL min^{-1}, while CO_2 was fed into the gas chamber at 5 mL min^{-1} (Figure S10). CO_2 permeating through the GDE was swept by the Ar stream to a gas chromatograph (GC) for quantification. The measured CO_2 permeabilities of the dry GDEs were comparable, 27.15 and 26.41 µL s^{-1} cm^{-2} for FSP Bi_2O_3 and EC Bi_2O_3, respectively, indicating similar CO_2 flux through both electrodes and ensuring sufficient CO_2 supply to the compact catalyst layers.

EC CO_2 reduction performance

The ECO_2RR performance of the two Bi_2O_3 catalysts was evaluated under potentiostatic conditions in a microfluidic electrolyzer. Each potential was tested in triplicate for 1 h using a fresh electrode and electrolyte for every run. The average total current density (TCD) transients and their standard deviations were recorded (Figure S11, shaded areas indicate standard deviations). Bismuth is well known for its selectivity toward formate, with CO and H_2 as the only common side products.[22,53] The Faradaic efficiency (FE) and PCD for formate are shown in Figures 3A and 3B. For EC Bi_2O_3, $FE_{formate}$ exceeded 90% between −0.6 and −1.2 V vs. RHE, reaching a maximum of 96% at −1.0 V vs. RHE, while $PCD_{formate}$ increased from −60 to −336 mA cm^{-2}. FSP Bi_2O_3 exhibited superior performance, extending the high-selectivity window to −0.6 to −1.6 V vs. RHE and achieving a maximum $FE_{formate}$ of 98% at −0.8 V vs. RHE. Although both catalysts displayed similar $PCD_{formate}$ up to −0.8 V vs. RHE, FSP Bi_2O_3 showed higher activity at more negative potentials, reaching −600 mA cm^{-2} at −1.6 V vs. RHE. In contrast, for EC Bi_2O_3, the $FE_{formate}$ decreased to 68%, with $PCD_{formate}$ capped at −400 mA cm^{-2} and a continuous increase in the hydrogen evolution reaction (HER) (Figure 3C). For FSP Bi_2O_3, the onset of performance loss at high current densities was shifted by >200 mV to more negative potentials, yielding an $FE_{formate}$ of 75% at −2.0 V vs. RHE while maintaining a high $PCD_{formate}$ of −700 mA cm^{-2}. The full product distributions and corresponding PCD values for each potential and catalyst are summarized in Tables S1 and S2.

Both catalysts exhibited similar current densities in the potential range from −0.4 to −1.0 V vs. RHE, whereas at higher overpotentials, the FSP-based GDE sustained substantially higher current densities. This behavior suggests that the enhanced activity of the FSP GDE cannot be attributed solely to a higher surface area. It should also be noted that determining the electrochemically active surface area (ECSA) during electrolysis can be complicated by the conductive carbon-based GDE substrate and that *ex situ* ECSA measurements may not accurately represent the catalytically active area, since bismuth undergoes a phase transition from Bi_2O_3 to bismuth subcarbonate under reaction conditions.

The stability of the system is also reflected in the total current transients. Within the stable cathodic potential window, the current remained essentially constant over the 1 h electrolysis, whereas at potentials more negative than this window, the current steadily decayed (Figure S11). For FSP Bi_2O_3, current densities above −1 A cm^{-2} were sustained during the first 20 min of electrolysis, followed by a gradual decrease to around −750 mA cm^{-2}. Post-electrolysis surface SEM revealed a partial morphological transformation into larger sheets (Figure S12), which contributed to the observed loss in catalytic activity. The stability of the catalyst layer was further assessed by ICP-MS quantification of dissolved Bi^{3+} in the catholyte (Figure 3D; Table S3).

Within the stable potential window, both catalyst layers remained largely intact, with <1.5% of the initial Bi loading dissolved; this value also includes the initial conversion of Bi_2O_3 to bismuth subcarbonate. Surface SEM images after electrolysis showed continuous films (Figure S13), consistent with the ICP-MS results. At more negative potentials, vigorous hydrogen evolution destabilized the catalyst layer. While FSP Bi_2O_3 maintained mechanical integrity down to −1.6 V vs. RHE, the EC Bi_2O_3 GDE exhibited a 10%–20% loss of its initial catalyst loading, attributable to roughening of the catalyst film and morphological changes of the flake structure. The FSP Bi_2O_3 GDE showed similar behavior only under harsher conditions: it remained intact at −1.8 V vs. RHE, whereas at −2.0 V, substantial catalyst detachment was observed (Table S3). Overall, the more compact FSP Bi_2O_3 catalyst layer was significantly more resistant to hydrogen evolution-induced degradation as compared to EC Bi_2O_3.

The impact of GDE flooding on EC performance was evaluated by quantifying potassium perspiration collected in the trap located at the CO_2 outlet (experimental setup in Figure S14). At low overpotentials, both catalysts resisted flooding, and only minor perspiration was detected (Figure 3E; Table S4). Under these conditions, stable operation indicates that CO_2 mass transport remained sufficient to sustain PCD values above −300 mA cm^{-2}. At more negative potentials, electrowetting became increasingly pronounced, leading to a rapid increase in perspiration. While FSP Bi_2O_3 GDEs effectively suppressed electrolyte breakthrough down to −1.6 V vs. RHE, EC Bi_2O_3 showed a stronger rise in perspiration. This behavior is consistent with previous reports,[30,31,49] in which severe GDE flooding increases the CO_2 diffusion path length, limits mass transport, and ultimately causes performance degradation and enhanced H_2 evolution. GDE flooding can also be probed by tracking the Bi phase composition, since insufficient CO_2 supply at the catalyst surface promotes the conversion of bismuth subcarbonate into metallic bismuth.[29] The crystal structure of the active catalyst region after electrolysis was characterized by XRD, and the phase composition was quantified via Rietveld refinement to resolve potential-dependent changes. The detected Bi_2O_3 fraction likely results from post-electrolysis oxidation of metallic Bi under ambient conditions and is therefore incorporated into the metallic Bi fraction. As shown in Figure 3F, the low content of Bi^0 indicates that bismuth subcarbonate predominates at low overpotentials. With increasing cathodic potential, the metallic character of both catalysts increases.[54]

For both catalysts, the metallic Bi content increases at more negative cathodic overpotentials. In parallel, the $(BiO)_2CO_3$ reflexes decrease in intensity and broaden with increasing overpotential, indicating a restructuring of the flakes into smaller particles, as seen in the diffractograms (Figure S15).[55] The pronounced increase in the metallic phase at the most negative potentials is consistent with severe GDE flooding and the associated loss of CO_2 mass transfer to the catalyst, in agreement with previous reports.[29] The *in situ* Bi phase transition also affects GDE wettability. Post-electrolysis hydrophobicity was assessed using sessile-drop CA measurements. For applied potentials up to −1.6 V vs. RHE, bismuth subcarbonate films were hydrophilic, with CAs below 35°. Example images for different potentials and average CAs are depicted in Figures S16A and S16B. At more negative potentials, the increasing fraction of metallic bismuth made the surfaces progressively more hydrophobic. Exceptions were observed for electrodes with cracks or holes in the catalyst layer, where droplets were rapidly drawn into the GDL by capillary action. This effect is more pronounced for the EC Bi_2O_3 layer at −1.6 V vs. RHE due to the surface inhomogeneity (Figure S16C). Overall, maintaining the hydrophobic character of carbon-based GDLs remains challenging for robust electrolyte management.

Another advantage of the FSP method is its suitability for mass production, bringing it closer to industrial requirements. For the potential-dependent experiments, only a single batch of FSP-derived Bi_2O_3 precursor was required, whereas multiple EC Bi_2O_3 batches had to be prepared to complete all measurements. To evaluate the reproducibility of the FSP-derived electrocatalyst, a second control batch of FSP Bi_2O_3 was synthesized and subjected to the same potential-dependent tests (Figure S17). Both batches exhibited comparable EC performance, with selectivities and activities within experimental error. The control batch displayed less electrolyte perspiration and catalyst dissolution at potentials more negative than −1.4 V vs. RHE. These deviations are attributed to differences in the hydrogen evolution rate, which affect the mechanical stress on the catalyst layer and the pressure in the catholyte flow channel.

Considering the performance, degradation behavior, and structural evolution of the GDEs, the applied potential alone does not appear to be the primary cause of instability. Instead, the combined effects discussed above trigger earlier degradation in EC Bi_2O_3, driving it into a destructive cycle of flooding, enhanced hydrogen evolution, and catalyst loss at less negative cathodic potentials than for FSP Bi_2O_3. The summary of potential-dependent degradation for FSP- and EC-derived GDEs is schematically shown in Figure S18.

Time-dependent electrolysis and ICP-MS-assisted EDX profiling of perspired electrolyte

To further elucidate the degradation mechanism under flooding conditions, time-dependent potentiostatic electrolysis was conducted at −1.6 V vs. RHE. The evolution of catalytic selectivity and activity toward the main products is shown in Figures 4A and 4B. For FSP Bi_2O_3, $FE_{formate}$ decreased gradually from near unity to 81% over 1 h, whereas for EC Bi_2O_3, the selectivity dropped to 78% after only 20 min and further to 60% after 1 h. Both catalysts initially exhibited $PCD_{formate}$ exceeding −700 mA cm^{-2} during the first 10 min. Subsequently, FSP Bi_2O_3 maintained $PCD_{formate}$ above −600 mA cm^{-2} for the following 40 min, while the EC Bi_2O_3 current density decreased to −525 mA cm^{-2} after 20 min and to −325 mA cm^{-2} after 1 h. Over the same period, FSP Bi_2O_3 showed only a modest increase in FE_{H2} (to 15% after 1 h), in contrast to EC Bi_2O_3, for which FE_{H2} rose to 38% after 1 h. The increase in HER and associated vigorous bubble formation also promotes mechanical degradation of the catalyst layer. For EC Bi_2O_3, less than 10% of the initial Bi loading was lost during the first 40 min, followed by a sharp increase to ~50% after 60 min (Figure 4C; Table S5). In contrast, the FSP Bi_2O_3 catalyst layer remained essentially intact, with only 2.6% of the original Bi loading dissolved in the catholyte after 1 h,

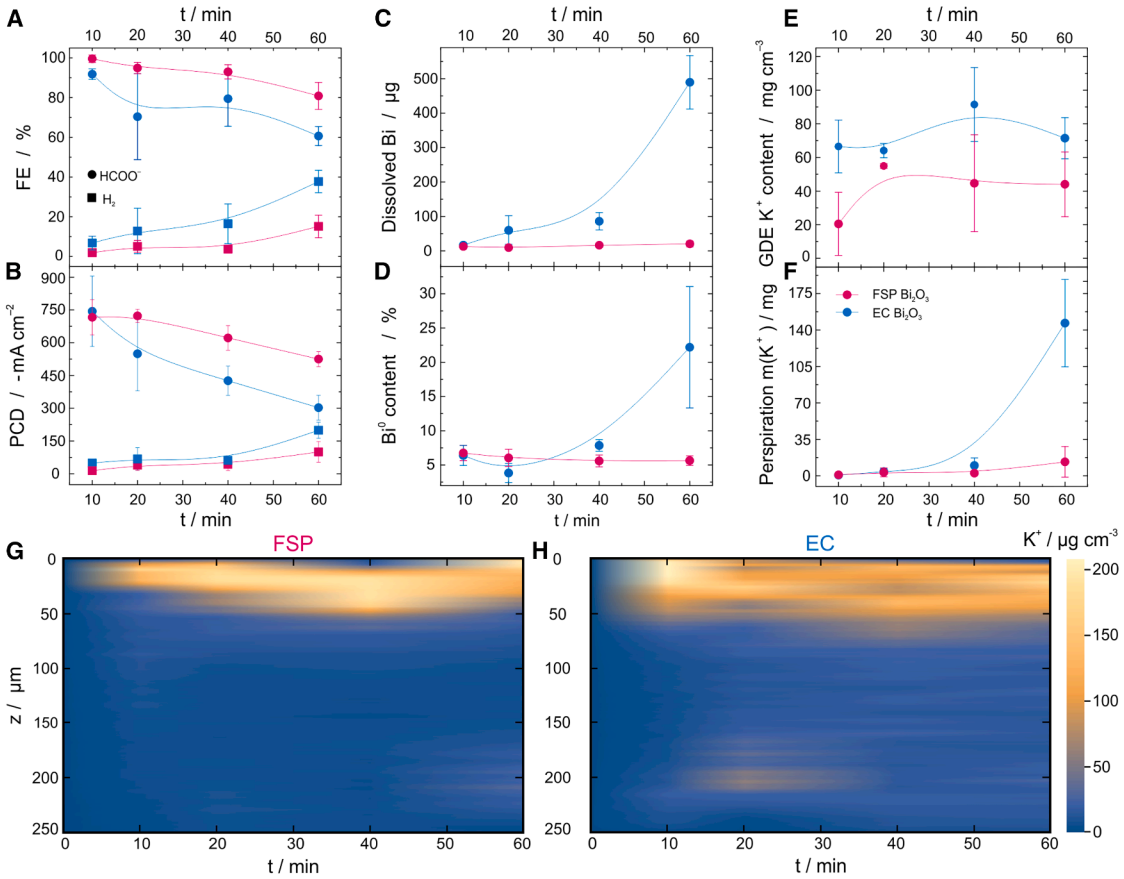

Figure 4. Time-dependent potentiostatic electrolysis at −1.6 V vs. RHE, with error bars indicating the standard deviations of three measurements

(A) Faradaic efficiencies of formate and H_2 for FSP Bi_2O_3 and EC Bi_2O_3. Data are represented as mean ± SEM (n = 3).

(B) Corresponding partial current densities. Data are represented as mean ± SEM (n = 3).

(C) Temporal evolution of dissolved Bi^{3+} in the catholyte, determined *ex situ* by ICP-MS. Data are represented as mean ± SEM (n = 3).

(D) The crystalline metallic Bi content obtained from full Rietveld refinement of *ex situ* XRD data. Data are represented as mean ± SEM (n = 3).

(E and F) Time-dependent amounts of K^+ in the perspired electrolyte and K^+ accumulated inside the GDE, quantified by ICP-MS. Data are represented as mean ± SEM (n = 3).

(G and H) Heatmaps of the temporal evolution of the localized K^+ concentration across the GDE cross-section.

demonstrating the superior stability of the compact layer. This trend is corroborated by surface SEM (Figure S19). Initially, both catalyst layers consisted of homogeneously stacked flakes of various sizes. With increasing operation time, the EC Bi_2O_3 films developed cracks and holes, and the morphology became progressively disrupted. Post-electrolysis XRD revealed that Bi_2O_3 was fully converted to $(BiO)_2CO_3$ within the first 10 min of electrolysis (Figure 4D; Table S6). While the FSP Bi_2O_3 catalyst layer maintained an essentially constant phase composition over 1 h, the EC Bi_2O_3 films were further reduced to metallic Bi^0 after 40 min of operation.

To investigate the time-dependent evolution of flooding, the potassium concentration in both the perspired catholyte and within the GDE was quantified and spatially resolved using ICP-MS EDX cross-sectional profiling (Figures S20 and S21).[28,56] As shown in Figure 4E, the average K^+ concentration in the FSP Bi_2O_3 GDE remained consistently lower than in EC Bi_2O_3. FSP Bi_2O_3 exhibited an initial saturation behavior during the first 20 min, consistent with a delayed onset of electrolyte perspiration (Figures 4F and S22). In both systems, most perspiration occurred during the final third of the experiment. At early times, both catalysts showed limited perspiration, but EC Bi_2O_3 displayed more electrolyte breakthrough due to its less compact catalyst layer and the development of a more porous structure, as seen in surface SEM (Figure S19). During the first 10 min, the flow channel became saturated, and only small amounts of K^+ reached the trap. ICP-MS EDX cross-sectional profiling heatmaps show that, for both catalysts, most salts were localized at the top of the catalyst layer and within the MPL, corresponding to the first ~50 µm of the depth profiles (Figures 4G and 4H). The heatmaps were constructed from average concentration depth profiles (shown in Figure S23A), obtained by analyzing two different electrodes at three distinct locations on each electrode. Interestingly, the pronounced salt accumulation on the EC Bi_2O_3 catalyst layer after 10 min of electrolysis indicates that the catalyst layer remained largely intact, limiting deeper electrolyte penetration into the

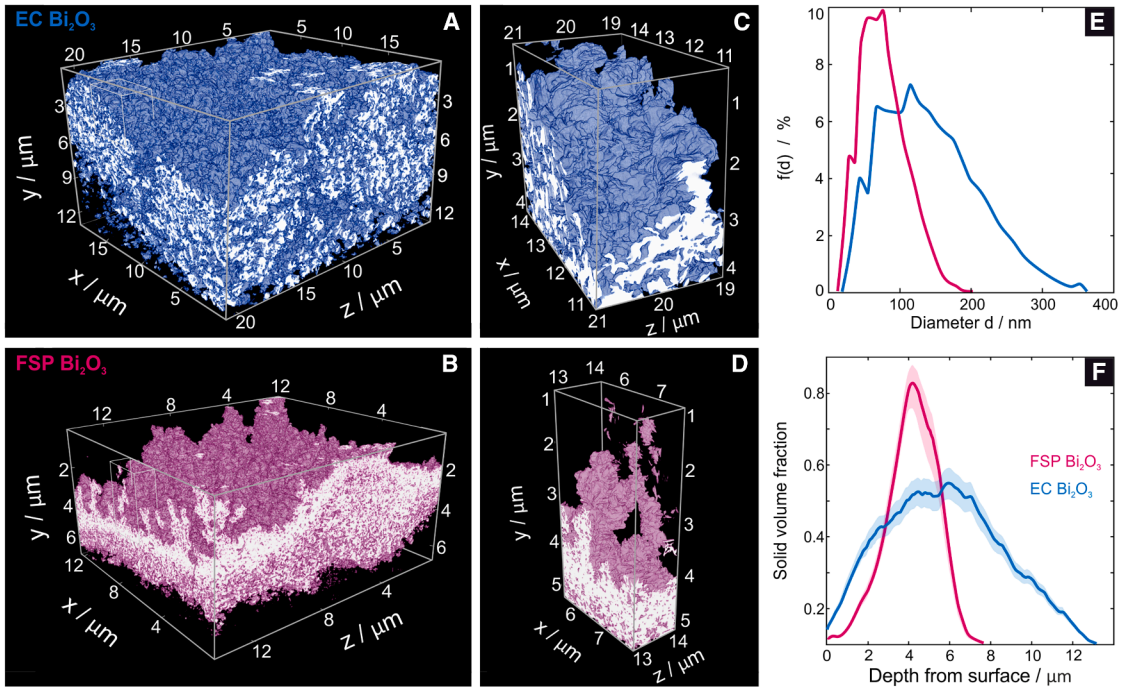

Figure 5. FIB-SEM nano-tomography of EC Bi_2O_3 and FSP Bi_2O_3 catalyst layers

(A and B) 3D reconstructions of the EC and FSP Bi_2O_3 catalyst layers.

(C and D) Close-up views of the 3D models highlighting the primary structural units forming the catalyst films.

(E) Particle size density function with the corresponding particle size distribution shown in the inset.

(F) Solid volume fraction as a function of distance from the MPL.

GDL, consistent with the surface SEM observations. As the FSP-gained catalyst layer was stable over the complete measurement, the majority of the salt precipitation was detected on the top of the catalyst surface.

Over time, gradual electrolyte ingress through the GDE increased the hydrophilicity of the substrate.[57,58] This saturation behavior was particularly evident in the MPL of the FSP Bi_2O_3 GDE, which became progressively wetted during the first 20 min. Because $PCD_{formate}$ remained constant over this period, CO_2 mass transport was not significantly impeded despite the increased diffusion path length in the MPL. To resolve salt deposition in the CFL ($z > 50$ µm), ICP-MS-assisted EDX data were evaluated using a lower intensity scale (Figure S23B). Initially, both GDEs showed no salt within the CFL. After 20 min, however, the EC Bi_2O_3 GDE exhibited substantial salt accumulation in this region, coinciding with a 15% drop in formate selectivity and indicating hindered CO_2 mass transport. In contrast, the dense, compact FSP Bi_2O_3 layer retained most salt deposits near the GDE surface and effectively limited electrolyte penetration into the CFL during the first 40 min. Only at the end of electrolysis did minor salt deposits appear at the bottom of the GDE, supported by the observation of a noticeable increase in perspiration.

Immediately after electrolysis, the CO_2 permeability of the GDEs was *in-situ*-measured in the electrolyzer (Figure S24). After 10 min, the FSP Bi_2O_3 catalyst layer became highly compact, with substantial salt accumulation on its surface, reducing the CO_2 flux to <1 µL s^{-1} cm^{-2}, which was much lower than that of the fresh GDEs. As the experiment progresses, the permeability gradually increases due to catalyst layer porosity evolution resulting from electrolyte penetration. The additional CO_2 pathways increase the permeability above 3 µL s^{-1}. In contrast, the EC Bi_2O_3 catalyst layer remained more porous, leading to a more homogeneous salt distribution within the GDE and a higher CO_2 permeability of 5.8 µL s^{-1} cm^{-2} after 10 min. As material loss progressed and large holes and cracks formed, the permeability increased further to 7.4 µL s^{-1} cm^{-2}, before decreasing again when larger regions of the MPL became directly covered by potassium-based salts. It should be noted that the gas permeability measurements were conducted under gas/gas conditions and therefore do not directly represent the effective gas transport behavior under gas/liquid operational electrolysis conditions. Thus, the permeability values reported here are used as comparative descriptors of the intrinsic through-plane gas transport resistance of the wetted GDEs rather than as quantitative predictors of gas transport during operation.

Post-electrolysis FIB-SEM nano-tomography analysis

FIB-SEM nano-tomography was performed on electrodes after 1 h of electrolysis to further resolve catalyst layer evolution.[56] On the macroscopic scale, surface SEM images of EC Bi_2O_3 showed a porous structure with cracks extending down to the substrate. Figure 5A displays the FIB-SEM nano-tomography reconstruction of an intact EC Bi_2O_3 GDE section (~19 × 21 µm; corresponding size is marked in Figure S25A). The flat white regions in the 3D model represent cross-sectional cuts through the underlying Bi_2O_3 catalyst particles. In contrast,

surface SEM of FSP Bi_2O_3 revealed a compact layer composed of micrometer-sized flakes, clearly visible at the top of the 3D model in Figure 5B (area: ~12.4 × 13.9 μm, Figure S25B). The EC Bi_2O_3 catalyst layer consists of micrometer-sized, cauliflower-like agglomerates forming a continuous network. A close-up (Figure 5C) shows that these structures are built from smaller primary particles with an average diameter of 142 ± 11 nm (Figure 5E), with ~80% of the particles in the 55–230 nm range. The post-electrolysis FIB-SEM nano-tomography of the EC Bi_2O_3 catalyst layer showed a loosely packed cauliflower structure, different from what we previously observed for the as-prepared EC Bi_2O_3,[28] indicating the morphological evolution of EC Bi_2O_3 during electrolysis. By contrast, FSP Bi_2O_3 forms a compact layer of small particles extending down to the MPL. The converted FSP Bi_2O_3 particles appear as fine lamellae (Figure 5D) with an average diameter of 76 ± 11 nm, and ~80% of the particles lie between 34 and 117 nm, significantly smaller than for EC Bi_2O_3. The EC Bi_2O_3 catalyst layer appears relatively homogeneous and isotropic in all three directions on the micrometer scale, with a maximum chord length of 2.5 μm (Figure S25E). In contrast, the post-electrolysis FSP sample exhibits anisotropy along the *z* axis: chords in the *z* direction have a maximum length of 2.25 μm, whereas the longest chords in the *x* and *y* directions are ~4 μm (Figure S25F).

The solid volume fraction, defined as the total catalyst volume normalized to the geometric surface area, is plotted as a function of distance from the top of the MPL in Figure 5F. EC Bi_2O_3 forms a more extended catalyst layer (~13 μm) than FSP Bi_2O_3 (~8 μm), yet segmentation analysis shows that both samples possess similar overall mesoscale porosity and solid volume fractions (Table S7). Overall, the FIB-SEM nano-tomography data support the EC results and the superior flooding resistance of FSP Bi_2O_3 GDEs: the more compact FSP Bi_2O_3 layer is mechanically more robust than EC Bi_2O_3, which is consistent with its reduced surface wettability and improved electrolyte management observed by ICP-MS EDX cross-sectional profiling.

Long-term testing further demonstrates stable formate production at −200 mA cm^{-2} for 12 h, with H_2 selectivity remaining below 20%. Adding PTFE particles to the catalyst layer (50 wt % loading compared to the catalyst) extended stable operation to 33 h. Moreover, stable performance was sustained for 24 h at −400 mA cm^{-2} (Figure S26). During the galvanostatic electrolysis experiments, the applied potentials were in the range of −0.8 to −1.2 V vs. RHE. To investigate the influence of the additive on higher cathodic potentials and thus under enhanced electrowetting conditions, a time-dependent potentiostatic study was performed at −1.6 V vs. RHE. The large PTFE particles establish hydrophobic CO_2 transport pathways within the catalyst layer, resulting in enhanced mass transport and higher PCDs for formate production while maintaining comparable selectivity (see Figures S27A and S27B). However, with increasing electrolysis time, these hydrophobic pores gradually become blocked, causing the performance of the PTFE-reinforced FSP Bi_2O_3 GDE to converge toward that of the pristine FSP Bi_2O_3 GDE. This behavior is also reflected in the electrolyte management of the GDE (Figures S27C and S27D). During the first 20 min of electrolysis, electrolyte penetration was largely confined to the MPL (Figure S27F), and only negligible electrolyte perspiration was observed. Over the remainder of the experiment, the electrolyte content within the CFL steadily increased, while perspiration remained low. The addition of PTFE therefore reduced electrolyte perspiration through the GDE, leading to electrolyte accumulation within the CFL and consequently reduced CO_2 mass transport.

The results of this study highlight the critical influence of catalyst morphology on electrolyte management in GDEs, complementing the extensive body of research focused on the development of highly active catalyst materials. Potentiostatic and time-dependent investigations revealed the superior performance of the small, spherical FSP-derived Bi_2O_3 precursor compared to the electrochemically deposited, micrometer-sized dendritic Bi_2O_3 precursor (summarized in Figures S18 and S28). FIB-SEM tomography showed that, although both catalyst precursors were converted into flake-like structures during operation, the FSP-derived Bi_2O_3 formed a significantly denser catalyst layer. Furthermore, ICP-MS EDX cross-sectional profiling demonstrated that this compact FSP Bi_2O_3 layer effectively restricted electrolyte penetration to the MPL, whereas the EC Bi_2O_3 electrode became fully wetted. However, the methods applied herein are limited by the analyzed size of the GDE and the required *ex situ* characteristics. Whereas ICP-MS EDX profiling covers a larger segment of a complete GDE cross-section, FIB-SEM tomography analyzes single micrometer-sized spots with high resolution and accuracy.

In this work, two bismuth oxide precursors with identical chemical composition were synthesized by DHBT electrodeposition and FSP. Despite their chemical similarity, the materials exhibited distinct morphologies and particle sizes: FSP yielded spherical nanoparticles (~10–100 nm), whereas the electrochemically derived Bi_2O_3 consisted of micrometer-sized dendritic structures. EC-derived Bi_2O_3 showed formate selectivity above 90% within a potential window of −0.6 to −1.2 V vs. RHE, while FSP-derived Bi_2O_3 maintained >90% selectivity over a wider range from −0.6 to −1.6 V vs. RHE. Moreover, FSP Bi_2O_3 reached a maximum PCD for formate of −700 mA cm^{-2}, outperforming the EC-derived catalyst (−396 mA cm^{-2}). The sharp decline in formate selectivity for EC Bi_2O_3 was attributed to mechanical instability of the catalyst layer and an earlier onset of a self-reinforcing degradation cycle involving material loss, increased hydrogen evolution, and electrode flooding. To elucidate these processes, FIB-SEM nano-tomography was combined with ICP-MS EDX cross-sectional profiling to track catalyst layer evolution and its interaction with flooding behavior in GDEs. EC Bi_2O_3 formed larger particles and degraded more rapidly into a porous structure, whereas FSP Bi_2O_3 developed a compact layer adjacent to the MPL. This compact morphology effectively confined flooding to the catalyst and microporous layers, enabling prolonged stable operation. These insights provide design guidelines for optimizing catalyst layers in CO_2 electroreduction and other gas-involving EC systems.

METHODS

Catalyst synthesis

The dendritic Bi catalyst was synthesized using the previously established two-step synthesis via DHBT electrodeposition. First, a highly porous Bi foam was deposited onto a Cu foil in a three-electrode setup under harsh galvanostatic conditions. In

a second step, the foam was mechanically detached, and the resulting metallic Bi particles were thermally oxidized at 350°C to the EC Bi_2O_3 catalyst. The spherical Bi_2O_3 catalyst was directly obtained with FSP preparation. A dissolved Bi precursor was dispersed as an aerosol and ignited by a methane/oxygen flame. The resulting FSP Bi_2O_3 nanoparticles were collected on glass fiber filters. Further details on the catalyst preparation methods are provided in supplemental methods.

GDE preparation

The Bi_2O_3 nanoparticles were dispersed in an isopropanol-based ink containing Nafion as a binder and, optionally, PTFE particles as a hydrophobic additive. After ultrasonication, the ink was spray coated onto a GDL using a nitrogen-driven airbrush under vacuum. A more specific description is presented in the supplemental methods.

EC setup and measurements

The electrolysis experiments were performed in a three-electrode flow cell, with a leakless Ag/AgCl reference electrode. Humidified CO_2 was supplied to the GDE, and 1 M KOH was recirculated through the cathode and anode compartments. The products were quantified by online gas chromatography and post-electrolysis liquid ion chromatography. A detailed description of all components and the required calculations can be found in the supplemental methods.

Characterization of the electrocatalysts and GDEs

The surface area of the freshly prepared particles was determined by nitrogen adsorption, and the particle size distribution was measured by DLS. The mesoscopic structures of the catalyst layer and its underlying nanomorphology were visualized using an optical 3D microscope, a white-light interferometer, SEM, and HRTEM. XRD was applied for the identification of the bulk crystal structure. The surface elemental and chemical composition was investigated by EDX mapping and Raman microscopy. Sessile-drop CA experiments were performed to study the hydrophobicity of the electrodes. Catalyst degradation and electrolyte management of the GDE were quantified by ICP-MS. Small sections of the GDEs were embedded in epoxy and characterized by FIB-SEM nano-tomography to obtain high-resolution 3D reconstructions of the catalyst layer. The image layers were segmented and analyzed to quantify key morphological properties of the catalyst layer. The local potassium salt distributions in the GDE were quantified by the previously established ICP-MS-assisted EDX profiling method. Cross-sections of the GDEs were analyzed by EDX mapping, and depth-dependent potassium profiles were extracted through image processing and subsequently calibrated using ICP-MS measurements of dissolved electrode samples. The applied conditions and the required instrumentation are detailed in the supplemental methods.

RESOURCE AVAILABILITY

Lead contact

Further information and requests for resources and reagents should be directed to and will be fulfilled by the lead contact, Hesamoddin Rabiee (hesamoddin.rabiee@unibe.ch).

Materials availability

This study did not generate new unique materials.

Data and code availability

- All data reported in this paper will be shared by the lead contact upon request.
- No code was generated in this study.
- Experimental data have been deposited at Zenodo (https://doi.org/10.5281/zenodo.17789939). Any additional information required to reanalyze the data reported in this paper is available from the lead contact upon request.

ACKNOWLEDGMENTS

This study was supported by NCCR Catalysis (grant numbers 180544 and 225147), a National Centre of Competence in Research funded by the Swiss National Science Foundation (SNSF) H.R. acknowledges support from the SNSF Postdoctoral Fellowship (SNSF SPF, grant no. 217305). L.W. is grateful for travel support from the Karlsruhe House of Young Scientists from the Karlsruhe Institute of Technology (KIT). S.V. acknowledges financial support from the Momentum Programme of the Hungarian Academy of Sciences (grant LP2022–18/2022).

AUTHOR CONTRIBUTIONS

A.R. synthesized the EC Bi_2O_3 particles; planned and performed the CO_2RR electrolysis experiments and the subsequent treatment and analysis of all the samples by SEM, ICP-MS-assisted EDX profiling, and CA measurements; designed the EC cell; developed the CO_2 permeability method; analyzed the data; and wrote the manuscript and supplemental methods. H.R. contributed to conceptualization, supervision, and writing and editing the manuscript and supplemental methods. F.L. planned and performed the FIB-SEM nano-tomography measurements, including the data analysis, and contributed to writing. P.W. synthesized the FSP Bi_2O_3 particles, planned and performed the STEM and BET analyses, and edited the manuscript and supplemental methods. L.W. performed the Rietveld refinement of the XRD data and edited the manuscript and supplemental methods. S.V. adjusted the code for the ICP-MS-assisted EDX profiling and edited the manuscript and supplemental methods. R.G., S.H., and P.B. edited the manuscript and supplemental methods and provided critical feedback to help shape the work.

DECLARATION OF INTERESTS

The authors declare no competing interests.

SUPPLEMENTAL INFORMATION

Supplemental information can be found online at https://doi.org/10.1016/j.xcrp.2026.103500.

Received: February 17, 2026
Revised: May 27, 2026
Accepted: July 28, 2026

REFERENCES

1. Mac Dowell, N., Fennell, P.S., Shah, N., and Maitland, G.C. (2017). The role of CO2 capture and utilization in mitigating climate change. Nat. Clim. Chang. *7*, 243–249. https://doi.org/10.1038/nclimate3231.
2. Rabiee, H., Dutta, A., Yan, P., Ge, L., Dorosti, F., Yu, X., Rieder, A., and Broekmann, P. (2025). From Flue Gas to Syngas: Composite Electrode Based on Ionic Liquid and Microporous Polymer for MEA-Based CO(2) Electrolysis. Angew. Chem. *64*, e202513103. https://doi.org/10.1002/anie.202513103.

3. Rabiee, H., Yan, P., Wang, H., Zhu, Z., and Ge, L. (2024). Electrochemical CO2 reduction integrated with membrane/adsorption-based CO2 capture in gas-diffusion electrodes and electrolytes. EcoEnergy *2*, 3–21. https://doi.org/10.1002/ece2.23.

4. Trivedi, V., Rajeshwaree, B., Biswas, R., Kashyap, M., Bhattacharya, S., and Dutta, A. (2025). Crafting sustainable CO2 electrolyzers. Cell Rep. Phys. Sci. *6*, 102790. https://doi.org/10.1016/j.xcrp.2025.102790.

5. Yu, X., Rabiee, H., Dutta, A., Li, Y., Szakály, Z., Vesztergom, S., Warmuth, L., Rieder, A., and Broekmann, P. (2025). Upcycling CO(2) and PET Waste: Ampere-Level Formate Electrosynthesis in an Integrated Electrolyzer. J. Am. Chem. Soc. *147*, 41481–41491. https://doi.org/10.1021/jacs.5c11708.

6. Hoof, L., Thissen, N., Pellumbi, K., junge Puring, K., Siegmund, D., Mechler, A.K., and Apfel, U.-P. (2022). Hidden parameters for electrochemical carbon dioxide reduction in zero-gap electrolyzers. Cell Rep. Phys. Sci. *3*, 100825. https://doi.org/10.1016/j.xcrp.2022.100825.

7. Ji, Y., Guan, A., and Zheng, G. (2022). Copper-based catalysts for electrochemical carbon monoxide reduction. Cell Rep. Phys. Sci. *3*, 101072–101094, ARTN 101072. https://doi.org/10.1016/j.xcrp.2022.101072.

8. McCallum, C., Gabardo, C.M., O'Brien, C.P., Edwards, J.P., Wicks, J., Xu, Y., Sargent, E.H., and Sinton, D. (2021). Reducing the crossover of carbonate and liquid products during carbon dioxide electroreduction. Cell Rep. Phys. Sci. *2*, 100522–100538. https://doi.org/10.1016/j.xcrp.2021.100522.

9. She, X., Zhang, T., Li, Z., Li, H., Xu, H., and Wu, J. (2020). Tandem Electrodes for Carbon Dioxide Reduction into C2+ Products at Simultaneously High Production Efficiency and Rate. Cell Rep. Phys. Sci. *1*, 100051–100065. https://doi.org/10.1016/j.xcrp.2020.100051.

10. Chen, G., Hong, M., Ma, B., Kuang, Y., Rabiee, H., Xu, X., Dorosti, F., Yan, P., Shah, N., Nanjundan, A.K., et al. (2026). Which dominates CO2 to CO electroreduction from low to industrial current density: Catalyst activity or CO2 availability? Appl. Catal. B Environ. Energy *381*, 125902. https://doi.org/10.1016/j.apcatb.2025.125902.

11. Zhang, J., Pham, T.H.M., Ko, Y., Li, M., Yang, S., Koolen, C.D., Zhong, L., Luo, W., and Züttel, A. (2022). Tandem effect of Ag@C@Cu catalysts enhances ethanol selectivity for electrochemical CO2 reduction in flow reactors. Cell Rep. Phys. Sci. *3*, 100949. https://doi.org/10.1016/j.xcrp.2022.100949.

12. Jiang, Y., Choi, C., Hong, S., Chu, S., Wu, T.-S., Soo, Y.-L., Hao, L., Jung, Y., and Sun, Z. (2021). Enhanced electrochemical CO2 reduction to ethylene over CuO by synergistically tuning oxygen vacancies and metal doping. Cell Rep. Phys. Sci. *2*, 100356. https://doi.org/10.1016/j.xcrp.2021.100356.

13. Rabiee, H., Zhang, X., Ge, L., Hu, S., Li, M., Smart, S., Zhu, Z., and Yuan, Z. (2020). Tuning the Product Selectivity of the Cu Hollow Fiber Gas Diffusion Electrode for Efficient CO2 Reduction to Formate by Controlled Surface Sn Electrodeposition. ACS Appl. Mater. Interfaces *12*, 21670–21681. https://doi.org/10.1021/acsami.0c03681.

14. Lei, P.-X., Liu, S.-Q., Wen, Q.-R., Wu, J.-Y., Wu, S., Wei, X., Feng, R., Fu, X.-Z., and Luo, J.-L. (2025). Integrated "Two-in-One" Strategy for High-Rate Electrocatalytic CO2 Reduction to Formate. Angew. Chem. Int. Ed. Engl. *64*, e202415726. https://doi.org/10.1002/anie.202415726.

15. Nørskov, J.K., Bligaard, T., Rossmeisl, J., and Christensen, C.H. (2009). Towards the computational design of solid catalysts. Nat. Chem. *1*, 37–46. https://doi.org/10.1038/nchem.121.

16. Rabiee, H., Ge, L., Zhang, X., Hu, S., Li, M., Smart, S., Zhu, Z., and Yuan, Z. (2021). Shape-tuned electrodeposition of bismuth-based nanosheets on flow-through hollow fiber gas diffusion electrode for high-efficiency CO2 reduction to formate. Appl. Catal. B Environ. *286*, 119945–119956. https://doi.org/10.1016/j.apcatb.2021.119945.

17. Ren, X., Liu, F., Wu, H., Lu, Q., Zhao, J., Liu, Y., Zhang, J., Mao, J., Wang, J., Han, X., et al. (2024). Reconstructed Bismuth Oxide through in situ Carbonation by Carbonate-containing Electrolyte for Highly Active Electrocatalytic CO2 Reduction to Formate. Angew. Chem. Int. Ed. Engl. *63*, e202316640. https://doi.org/10.1002/anie.202316640.

18. Dutta, A., Zelocualtecatl Montiel, I., Kiran, K., Rieder, A., Grozovski, V., Gut, L., and Broekmann, P. (2021). A Tandem (Bi2O3 → Bimet) Catalyst for Highly Efficient ec-CO2 Conversion into Formate: Operando Raman Spectroscopic Evidence for a Reaction Pathway Change. ACS Catal. *11*, 4988–5003. https://doi.org/10.1021/acscatal.0c05317.

19. Li, B., Chen, J., Wang, L., Xia, D., Mao, S., Xi, L., Liu, H., Ying, S., and Wang, Y. (2025). High-Performance Bi-Based Catalysts for CO_2 Reduction: In Situ Formation of $Bi/Bi_2O_2CO_3$ and Enhanced Formate Production. Adv. Sci. *12*, 2415616. https://doi.org/10.1002/advs.202415616.

20. Zhou, Y., Wang, K., Zheng, S., Cheng, X., He, Y., Qin, W., Zhang, X., Chang, H., Zhong, N., and He, X. (2024). Advancements in electrochemical CO2 reduction reaction: A review on CO2 mass transport enhancement strategies. Chem. Eng. J. *486*, 150169. https://doi.org/10.1016/j.cej.2024.150169.

21. Ge, L., Rabiee, H., Li, M., Subramanian, S., Zheng, Y., Lee, J.H., Burdyny, T., and Wang, H. (2022). Electrochemical CO2 reduction in membrane-electrode assemblies. Chem *8*, 663–692. https://doi.org/10.1016/j.chempr.2021.12.002.

22. O'Brien, C.P., Miao, R.K., Shayesteh Zeraati, A., Lee, G., Sargent, E.H., and Sinton, D. (2024). CO2 Electrolyzers. Chem. Rev. *124*, 3648–3693. https://doi.org/10.1021/acs.chemrev.3c00206.

23. Rabiee, H., Ge, L., Hu, S., Wang, H., and Yuan, Z. (2022). Microtubular electrodes: An emerging electrode configuration for electrocatalysis, bioelectrochemical and water treatment applications. Chem. Eng. J. *450*, 138476–138496. https://doi.org/10.1016/j.cej.2022.138476.

24. Rabiee, H., Ge, L., Zhang, X., Hu, S., Li, M., and Yuan, Z. (2021). Gas diffusion electrodes (GDEs) for electrochemical reduction of carbon dioxide, carbon monoxide, and dinitrogen to value-added products: a review. Energy Environ. Sci. *14*, 1959–2008. https://doi.org/10.1039/D0EE03756G.

25. Wu, Y., Garg, S., Li, M., Idros, M.N., Li, Z., Lin, R., Chen, J., Wang, G., and Rufford, T.E. (2022). Effects of microporous layer on electrolyte flooding in gas diffusion electrodes and selectivity of CO2 electrolysis to CO. J. Power Sources *522*, 230998. https://doi.org/10.1016/j.jpowsour.2022.230998.

26. Lai, W., Qiao, Y., Wang, Y., and Huang, H. (2023). Stability Issues in Electrochemical CO2 Reduction: Recent Advances in Fundamental Understanding and Design Strategies. Adv. Mater. *35*, 2306288. https://doi.org/10.1002/adma.202306288.

27. Wu, Y., Rabiee, H., Zhao, X.S., Wang, G., and Jiang, Y. (2024). Insights into electrolyte flooding in flexible gas diffusion electrodes for CO2 electrolysis: from mechanisms to effective mitigation strategies. J. Mater. Chem. A Mater. *12*, 14206–14228. https://doi.org/10.1039/d4ta01994f.

28. Rieder, A., Lorenzetti, J., Zelocualtecatl Montiel, I., Dutta, A., Iarchuk, A., Mirolo, M., Drnec, J., Lorenzutti, F., Haussener, S., Kovács, N., et al. (2024). ICP–MS Assisted EDX Tomography: A Robust Method for Studying Electrolyte Penetration Phenomena in Gas Diffusion Electrodes Applied to CO2 Electrolysis. Small Methods *8*, 2400200. https://doi.org/10.1002/smtd.202400200.

29. Zelocualtecatl Montiel, I., Dutta, A., Kiran, K., Rieder, A., Iarchuk, A., Vesztergom, S., Mirolo, M., Martens, I., Drnec, J., and Broekmann, P. (2022). CO2 Conversion at High Current Densities: Stabilization of Bi(III)-Containing Electrocatalysts under CO2 Gas Flow Conditions. ACS Catal. *12*, 10872–10886. https://doi.org/10.1021/acscatal.2c02549.

30. Kong, Y., Liu, M., Hu, H., Hou, Y., Vesztergom, S., Gálvez-Vázquez, M.d.J., Zelocualtecatl Montiel, I., Kolivoška, V., and Broekmann, P. (2022). Cracks as Efficient Tools to Mitigate Flooding in Gas Diffusion Electrodes Used for the Electrochemical Reduction of Carbon Dioxide. Small Methods *6*, 2200369. https://doi.org/10.1002/smtd.202200369.

31. Hu, H., Kong, Y., Liu, M., Kolivoška, V., Rudnev, A.V., Hou, Y., Erni, R., Vesztergom, S., and Broekmann, P. (2023). Effective perspiration is essential to uphold the stability of zero-gap MEA-based cathodes used in CO2 electrolysers. J. Mater. Chem. A Mater. *11*, 5083–5094. https://doi.org/10.1039/D2TA06965B.

32. Senocrate, A., Bernasconi, F., Rentsch, D., Kraft, K., Trottmann, M., Wichser, A., Bleiner, D., and Battaglia, C. (2022). Importance of Substrate Pore Size and Wetting Behavior in Gas Diffusion Electrodes for CO2 Reduction. Acs Appl Energ Mater *5*, 14504–14512. https://doi.org/10.1021/acsaem.2c03054.

33. Rabiee, H., Ma, B., Yang, Y., Li, F., Yan, P., Wu, Y., Zhang, X., Hu, S., Wang, H., Ge, L., and Zhu, Z. (2024). Advances and Challenges of Carbon-Free Gas-Diffusion Electrodes (GDEs) for Electrochemical CO2 Reduction. Adv. Funct. Mater. *35*, 2411195. https://doi.org/10.1002/adfm.202411195.

34. Rabiee, H., Li, M., Yan, P., Wu, Y., Zhang, X., Dorosti, F., Zhang, X., Ma, B., Hu, S., Wang, H., et al. (2024). Rational Designing Microenvironment of Gas-Diffusion Electrodes via Microgel-Augmented CO(2) Availability for High-Rate and Selective CO(2) Electroreduction to Ethylene. Adv. Sci. *11*, e2402964. https://doi.org/10.1002/advs.202402964.

35. Abarca, J.A., Warmuth, L., Rieder, A., Dutta, A., Vesztergom, S., Broekmann, P., Irabien, A., and Díaz-Sainz, G. (2025). GDE Stability in CO2 Electroreduction to Formate: The Role of Ionomer Type and Loading. ACS Catal. *15*, 8753–8767. https://doi.org/10.1021/acscatal.5c02052.

36. Xing, Z., Hu, L., Ripatti, D.S., Hu, X., and Feng, X. (2021). Enhancing carbon dioxide gas-diffusion electrolysis by creating a hydrophobic catalyst microenvironment. Nat. Commun. *12*, 136. https://doi.org/10.1038/s41467-020-20397-5.

37. Li, L., Zhang, X., Liu, C., Mosali, V.S.S., Chen, J., Bond, A.M., Gu, Q., and Zhang, J. (2023). Hydrophobicity graded gas diffusion electrode with enhanced CO intermediate coverage for high-performance electroreduction of CO2 to ethylene. Appl. Catal. B Environ. *331*, 122597. https://doi.org/10.1016/j.apcatb.2023.122597.

38. Jiang, Z., Lyu, Z.-H., Liu, X.-Z., Fu, J., Zhang, L., Yao, Z.-C., Zheng, L.-R., Su, D., Fan, Y.-J., Tang, T., and Hu, J.-S. (2025). Micro/Nano-Structured Superhydrophobic Gas Diffusion Electrode for Boosting the Stability of Industrial-Compatible Electrochemical CO Production in Flow Cells. Adv. Funct. Mater. *35*, 2401927. https://doi.org/10.1002/adfm.202401927.

39. Moss, A.B., Hätinen, J., Kúš, P., Garg, S., Mirolo, M., Chorkendorff, I., Seger, B., and Drnec, J. (2023). Versatile high energy X-ray transparent electrolysis cell for operando measurements. J. Power Sources *562*, 232754. https://doi.org/10.1016/j.jpowsour.2023.232754.

40. Xu, Q., Zamora Zeledón, J.A., Joensen, B.Ó., Trotochaud, L., Sartori, A., Kaas, L.M., Moss, A.B., Mirolo, M., Mairena, L., Huynh, S., et al. (2025). Operando X-ray characterization platform to unravel catalyst degradation under accelerated stress testing in CO2 electrolysis. Nat. Nanotechnol. *20*, 889–896. https://doi.org/10.1038/s41565-025-01916-1.

41. Rottmann, D.M., Kollmuss, R., Haufe, S., and Mayrhofer, K.J.J. (2025). In-Operando Quantification of Electrode Flooding in CO2 Electrolysis and Correlation to Product Distribution. J. Electrochem. Soc. *172*, 054510. https://doi.org/10.1149/1945-7111/add569.

42. Bi, T., Xue, R., Jiang, Y., Yuan, S., Zhao, C., Zhang, G., Cheng, X., Yin, J., Wei, G., Yan, X., and Zhang, J. (2024). Regulating water transport and salt precipitation for CO2RR by creating a functional layer. Int. J. Hydrogen Energy *90*, 784–791. https://doi.org/10.1016/j.ijhydene.2024.10.007.

43. Pellumbi, K., Krisch, D., Rettenmaier, C., Awada, H., Sun, H., Song, L., Sanden, S.A., Hoof, L., Messing, L., Puring, K.j., et al. (2023). Pushing the Ag-loading of CO2 electrolyzers to the minimum via molecularly tuned environments. Cell Rep. Phys. Sci. *4*, 101746. https://doi.org/10.1016/j.xcrp.2023.101746.

44. Vesztergom, S., Dutta, A., Rahaman, M., Kiran, K., Zelocualtecatl Montiel, I., and Broekmann, P. (2021). Hydrogen Bubble Templated Metal Foams as Efficient Catalysts of CO2 Electroreduction. ChemCatChem *13*, 1039–1058. https://doi.org/10.1002/cctc.202001145.

45. Teoh, W.Y., Amal, R., and Mädler, L. (2010). Flame spray pyrolysis: An enabling technology for nanoparticles design and fabrication. Nanoscale *2*, 1324–1347. https://doi.org/10.1039/C0NR00017E.

46. Pinheiro Araújo, T., Morales-Vidal, J., Zou, T., García-Muelas, R., Willi, P.O., Engel, K.M., Safonova, O.V., Faust Akl, D., Krumeich, F., Grass, R.N., et al. (2022). Flame Spray Pyrolysis as a Synthesis Platform to Assess Metal Promotion in In2O3-Catalyzed CO2 Hydrogenation. Adv. Energy Mater. *12*, 2103707. https://doi.org/10.1002/aenm.202103707.

47. Gröhn, A.J., Pratsinis, S.E., Sánchez-Ferrer, A., Mezzenga, R., and Wegner, K. (2014). Scale-up of Nanoparticle Synthesis by Flame Spray Pyrolysis: The High-Temperature Particle Residence Time. Ind. Eng. Chem. Res. *53*, 10734–10742. https://doi.org/10.1021/ie501709s.

48. Grass, R.N., and Stark, W.J. (2006). Flame spray synthesis under a non-oxidizing atmosphere: Preparation of metallic bismuth nanoparticles and nanocrystalline bulk bismuth metal. J. Nanopart. Res. *8*, 729–736. https://doi.org/10.1007/s11051-006-9097-2.

49. Liu, M., Hu, H., Kong, Y., Montiel, I.Z., Kolivoška, V., Rudnev, A.V., Hou, Y., Erni, R., Vesztergom, S., and Broekmann, P. (2023). The role of ionomers in the electrolyte management of zero-gap MEA-based CO2 electrolysers: A Fumion vs. Nafion comparison. Appl. Catal. B Environ. *335*, 122885. https://doi.org/10.1016/j.apcatb.2023.122885.

50. Rabiee, H., Ge, L., Zhao, J., Zhang, X., Li, M., Hu, S., Smart, S., Rufford, T.E., Zhu, Z., Wang, H., and Yuan, Z. (2022). Regulating the reaction zone of electrochemical CO2 reduction on gas-diffusion electrodes by distinctive hydrophilic-hydrophobic catalyst layers. Appl. Catal. B Environ. *310*, 121362–121372. https://doi.org/10.1016/j.apcatb.2022.121362.

51. Varela, A.S. (2022). Effect of the reaction environment on the CO2 electrochemical reduction. Chem Catal. *2*, 233–235. https://doi.org/10.1016/j.checat.2022.01.009.

52. Sari, A., Al Maskari, N.S., Saeedi, A., and Xie, Q. (2020). Impact of surface roughness on wettability of oil-brine-calcite system at sub-pore scale. J. Mol. Liq. *299*, 112107. https://doi.org/10.1016/j.molliq.2019.112107.

53. Kuang, Y., Rabiee, H., Ge, L., Rufford, T.E., Yuan, Z., Bell, J., and Wang, H. (2023). High-Concentration Electrosynthesis of Formic Acid/Formate from CO2: Reactor and Electrode Design Strategies. Energy Environ. Mater. *6*, e12596. https://doi.org/10.1002/eem2.12596.

54. Weng, C., Wang, C., Song, Y., Zhang, Y.-X., Zou, K., Chen, H., Yang, X., and Lin, W. (2025). In-situ reconstruction of active bismuth for enhanced CO2 electroreduction to formate. Chem. Eng. J. *505*, 159732. https://doi.org/10.1016/j.cej.2025.159732.

55. Holder, C.F., and Schaak, R.E. (2019). Tutorial on Powder X-ray Diffraction for Characterizing Nanoscale Materials. ACS Nano *13*, 7359–7365. https://doi.org/10.1021/acsnano.9b05157.

56. Kong, Y., Hu, H., Liu, M., Hou, Y., Kolivoška, V., Vesztergom, S., and Broekmann, P. (2022). Visualisation and quantification of flooding phenomena in gas diffusion electrodes used for electrochemical CO2 reduction: A combined EDX/ICP–MS approach. J. Catal. *408*, 1–8. https://doi.org/10.1016/j.jcat.2022.02.014.

57. Gyenes, P., Samu, A.A., Hursán, D., Józó, V., Serfőző, A., Endrődi, B., and Janáky, C. (2025). Flooding revisited: electrolyte management ensures robust electrochemical CO2 reduction. Energy Environ. Sci. *18*, 7124–7135. https://doi.org/10.1039/d5ee01464f.

58. Zhang, T., Li, Z., Lyu, X., Raj, J., Zhang, G., Kim, H., Wang, X., Chae, S., Lemen, L., Shanov, V.N., and Wu, J. (2022). The Conventional Gas Diffusion Electrode May Not Be Resistant to Flooding during CO2/CO Reduction. J. Electrochem. Soc. *169*, 104506. https://doi.org/10.1149/1945-7111/ac9b96.